

Semi-automatic mapping of geological Structures using UAV-based photogrammetric data: An image analysis approach



Yathunanthan Vasuki*, Eun-Jung Holden, Peter Kovesi, Steven Micklethwaite

Centre for Exploration Targeting, The University of Western Australia, 35 Stirling Highway, Crawley, WA 6009, Australia

ARTICLE INFO

Article history:

Received 1 October 2013

Received in revised form

14 April 2014

Accepted 16 April 2014

Available online 25 April 2014

Keywords:

Semi-automated fault mapping

Photogrammetric data analysis

Automated image feature detection

Contrast invariant feature detection

ABSTRACT

Recent advances in data acquisition technologies, such as Unmanned Aerial Vehicles (UAVs), have led to a growing interest in capturing high-resolution rock surface images. However, due to the large volumes of data that can be captured in a short flight, efficient analysis of this data brings new challenges, especially the time it takes to digitise maps and extract orientation data.

We outline a semi-automated method that allows efficient mapping of geological faults using photogrammetric data of rock surfaces, which was generated from aerial photographs collected by a UAV. Our method harnesses advanced automated image analysis techniques and human data interaction to rapidly map structures and then calculate their dip and dip directions. Geological structures (faults, joints and fractures) are first detected from the primary photographic dataset and the equivalent three dimensional (3D) structures are then identified within a 3D surface model generated by structure from motion (SfM). From this information the location, dip and dip direction of the geological structures are calculated.

A structure map generated by our semi-automated method obtained a recall rate of 79.8% when compared against a fault map produced using expert manual digitising and interpretation methods. The semi-automated structure map was produced in 10 min whereas the manual method took approximately 7 h. In addition, the dip and dip direction calculation, using our automated method, shows a mean \pm standard error of $1.9^\circ \pm 2.2^\circ$ and $4.4^\circ \pm 2.6^\circ$ respectively with field measurements. This shows the potential of using our semi-automated method for accurate and efficient mapping of geological structures, particularly from remote, inaccessible or hazardous sites.

© 2014 Elsevier Ltd. All rights reserved.

1. Introduction

Knowledge of geological structures and their topological relationships (e.g., faults, joints, igneous contacts, and unconformities) is important for a wide range of geosciences research and industry including mineral exploration, CO₂ sequestration, groundwater, and geothermal energy. Possibly the most basic dataset used to capture information on geological structures is the geological map. Structural maps typically show the location, geometry, orientation and trace length of structures of interest. Further information typically captured may also include across-strike spacing, roughness and density (Priest, 1993). The most fundamental of these properties are location, surface geometry and orientation because these properties are critical components of widely used techniques such as two dimensional (2D) cross-section construction, cross-section balancing, three dimensional (3D) visualisation of geology

and modelling of geophysical data. In order to obtain the highest resolution data, traditional field techniques include interpretations from photo mosaics or grid mapping. Such approaches can generate abundant and high quality data but can take weeks, even months, to complete.

With recent advances in aerial data acquisition technologies from aircraft and UAVs (Harwin and Lucieer, 2012; Turner et al., 2012), it is now possible to capture high-resolution rock surface images and analyse geological structures within those datasets digitally. Very large digital datasets can be collected rapidly, covering significant surface areas with centimetre-scale resolution in a matter of minutes.

Photogrammetry is a technique that captures 3D information of features from two or more photographs of the same object, obtained from different angles (Donovan and Lebaron, 2009; Haneberg, 2008; Linder, 2009). In particular, structure from motion (SfM), is a photogrammetric technique, where the camera positions and orientation are solved automatically, in contrast to conventional photogrammetry where a priori knowledge of these parameters is required (Snavey et al., 2007). SfM uses overlapping photos to construct 3D point clouds, from which it is relatively, straight-forward to calculate surface models

* Corresponding author. Tel.: +61 8 6488 1873; fax: +61 8 6488 1178.

E-mail addresses: yathunanthan.vasuki@research.uwa.edu.au (Y. Vasuki), eun-jung.holden@uwa.edu.au (E.-J. Holden), peter.kovesi@uwa.edu.au (P. Kovesi), steven.micklethwaite@uwa.edu.au (S. Micklethwaite).

such as wireframes or digital elevation models (DEMs) and finally generate orthorectified photomosaics or textured surfaces. With the advent of this technique it is now important to develop methods to analyse the resulting data rapidly and effectively.

Several studies used photogrammetric data to map and measure geological structures (Ferrero et al., 2009, 2011; Kottenstette, 2005). Kottenstette (2005) conducted a study to demonstrate the application of photogrammetric methods to map the locations of geological joints. Ferrero et al. (2009) compared the orientations of geological features (dip and dip direction) derived, from both a field survey and results from a photogrammetric study. Their results show a good agreement with field measurements. There are also commercially available close range photogrammetry software namely Sirovision, ShapeMetrix3D and 3DM Analyst, which are available to calculate the orientation of discontinuities (Haneberg, 2008; Tonon and Kottenstette, 2006). However, the studies mentioned above used manual interpretation to identify each individual structure in the photogrammetric models.

Visual interpretation is a subjective and time consuming process and this is highly dependent on human experience and ability (Hung et al., 2005). Subjectivity is involved in lineament identification and the true extends of it. For example, visual interpretation produces results which are mostly non-reproducible because different interpreters will have different levels of expertise or may use different identification criteria (Sander et al., 1997). Even the same observer does not reproduce all the lineaments in the same locations in multiple trials (Mabee et al., 1994). Such subjectivity can be minimised by integrating results from multiple observers or by employing a single observer across multiple trials (Mabee et al., 1994; Sander et al., 1997). However, both solutions can incur significant man-hours to derive an interpretation.

Automated feature detection in images is an active area of research in image processing, including many applications such as road extraction (Shao et al., 2011; Treash and Amaralunga, 2000) and medical applications (Den Hertog et al., 2010; Mulrane et al., 2008; Onkaew et al., 2011). Image analysis techniques provide an effective and fast method of lineament detection and these techniques can extract lineaments which are difficult to recognise using the human eye alone (Wang and Howarth, 1990). The main advantage of automated or semi-automated lineament detection is speed.

Several studies have reported on automatic geological structure detection from remote sensing images. Wu and Lee (2007) detected edges from satellite images using the Likelihood ratio edge detector, which was originally proposed by Oliver et al. (1996) and mathematical morphology techniques were used to join the edges. The Hough transform (Duda and Hart, 1972) has also been used to successfully detect lineaments (Argialas and Mavrantza, 2004; Vassilas et al., 2002; Wang and Howarth, 1990). Wang and Howarth (1990) conducted an experiment, where an expert manually mapped faults from the

images and these results were compared to the output from the automated analysis method and an available geological map. It was found that the visual method identified approximately 50% of faults, while the automated method detected 53.7–69.2% of the faults based on the threshold. Thus, the performance of automated methods can be equivalent to, or slightly more effective than visual interpretations for the detection of lineaments.

However there are some limitations in the previous studies. In automated methods optimum parameter selection according to different contrasts and different terrains is very crucial (Argialas and Mavrantza, 2004). Moreover automated methods often detect lineament like features which are related to non-geological structures such as power lines, roads and man-made features. Thus automated methods detect significantly more features than the actual features present in the study area (Abdullah et al., 2013; Sarp, 2005). These false positives needed to be edited and/or removed to produce a final map which is time consuming (Gustafsson, 1994). The identification of a single structure (fault) as a series of discontinuous line segments is another drawback of the automated lineament detection method (Abdullah et al., 2013; Sarp, 2005). The limitations of automated methods show that some degree of user interaction is required to produce a better structure map.

To overcome these limitations, Lemy and Hadjigeorgiou (2003) used artificial neural networks to separate the actual feature segments from the false positives detected by their automated method. The discontinuous segments were then manually joined together to form the final feature map. In our study we address this challenge by introducing contrast invariant edge detection algorithms to minimise the difficulty of parameter selection. We then incorporate user inputs into the segment linking process to avoid the detection of false positives and to produce more realistic results. The detected structures are automatically located within the corresponding 3D surface models. Then the orientation (dip and dip direction) and location of geological structures are calculated using automated methods. Our preliminary study showed the effectiveness of using advanced image analysis techniques to detect geological structures from photographs (Vasuki et al., 2013).

2. Data acquisition

UAVs are already widely used for a variety of purposes, including the digital reconstruction of architecture (Irschara et al., 2010) and for mapping moss beds to monitor climate changes (Harwin and Lucieer, 2012; Lucieer et al., 2011, 2013). For this study an eight-rotor oktokopter (Fig. 1a) was used to capture approximately 140 photographs at an altitude of 30–40 m at Piccaninny Point on the east coast of Tasmania, Australia. This low altitude flight resulted in high



Fig. 1. (a) Oktokopter Micro-UAV, fitted with Canon 550D digital SLR Camera. (b) Densified point cloud generated from UAV images using photogrammetry.

resolution photographs (1 pixel \approx 1 cm), covering a 100 m by 80 m area during a 5 min flight. The images captured a layered meta-sedimentary sequence cross-cut by a series of dikes and faults, as described in Micklithwaite et al. (2012).

For this study, the point cloud (Fig. 1b), which is a set of feature points in a 3D coordinate system was created using SfM techniques, following the methodology of Harwin and Lucieer (2012) and Lucieer et al. (2011). The Bundler software package (Snavely et al., 2007) was used to create a sparse point-cloud. Feature points were identified by the Scale-invariant feature transform (SIFT) algorithm (Lowe, 2004) and they were matched using approximate nearest neighbour *kd*-tree approach. The RANSAC algorithm filtered out poor matches and finally bundle block adjustment was used to calculate the 3D coordinates of each feature. This sparse point cloud was used as an input to Patch View Multi-Stereo (PMVS2) software (Furukawa and Ponce, 2010) and a dense point cloud was created. Finally, the point cloud coordinate system was transformed to the real world coordinate system and a digital elevation model (DEM) generated (Fig. 2a). The individual photos were georeferenced and stitched together to generate a single mosaic as shown in Fig. 2b (Turner et al., 2012). The relative accuracy of the dataset is in the order of 10–25 cm.

2.1. Our workflow on the analysis of photogrammetry data

Our method adds value to traditional survey methods and provides objective and consistent results that can be queried and reproduced. Our workflow consists of three steps as shown in Fig. 3. Firstly we mapped geological structures using semi-automated image analysis of the photographic dataset. Secondly, following identification of the corresponding 3D geological structure coordinates from the DEM, the best-fit plane coefficients are computed. Finally the dip and dip direction of the structure planes

are calculated. In the following sections we describe the techniques used in each of these steps.

3. User guided fault map generation

The workflow of structure detection in photographs is outlined in Fig. 4a. MATLAB code was developed for the structure mapping and Fig. 4b shows the graphical user interface of the tool and the parameters associated with each step. Each step and the corresponding parameters are described in detail in the following subsections. The parameters shown in Fig. 4 are the parameters used to detect the structures from the image (Fig. 5) presented in this paper.

3.1. Feature detection

Conventional edge detection techniques detect edges by identifying the points in the image, where the image intensity changes sharply. There are many existing methods to detect edges such as Canny, Sobel, Prewitt, Robert and the Laplacian of Gaussian. When the performance of these widely used spatial domain edge detection methods was compared, the results showed that the Canny (1986) method performs well and is able to detect strong and weak edges (Juneja and Sandhu, 2009; Maini and Aggarwal, 2009; Marghany et al., 2006). Alternatively, edges can be detected using measures that are invariant to image contrast and illuminations (Kovesi, 1999). In our study we investigate phase symmetry, phase congruency and Canny methods to detect edges within photogrammetric data.

Phase symmetry (Kovesi, 1997) is a feature detection technique for ridges or valleys, i.e., line like features. This algorithm is already used in geology and geophysics to detect regions of magnetic

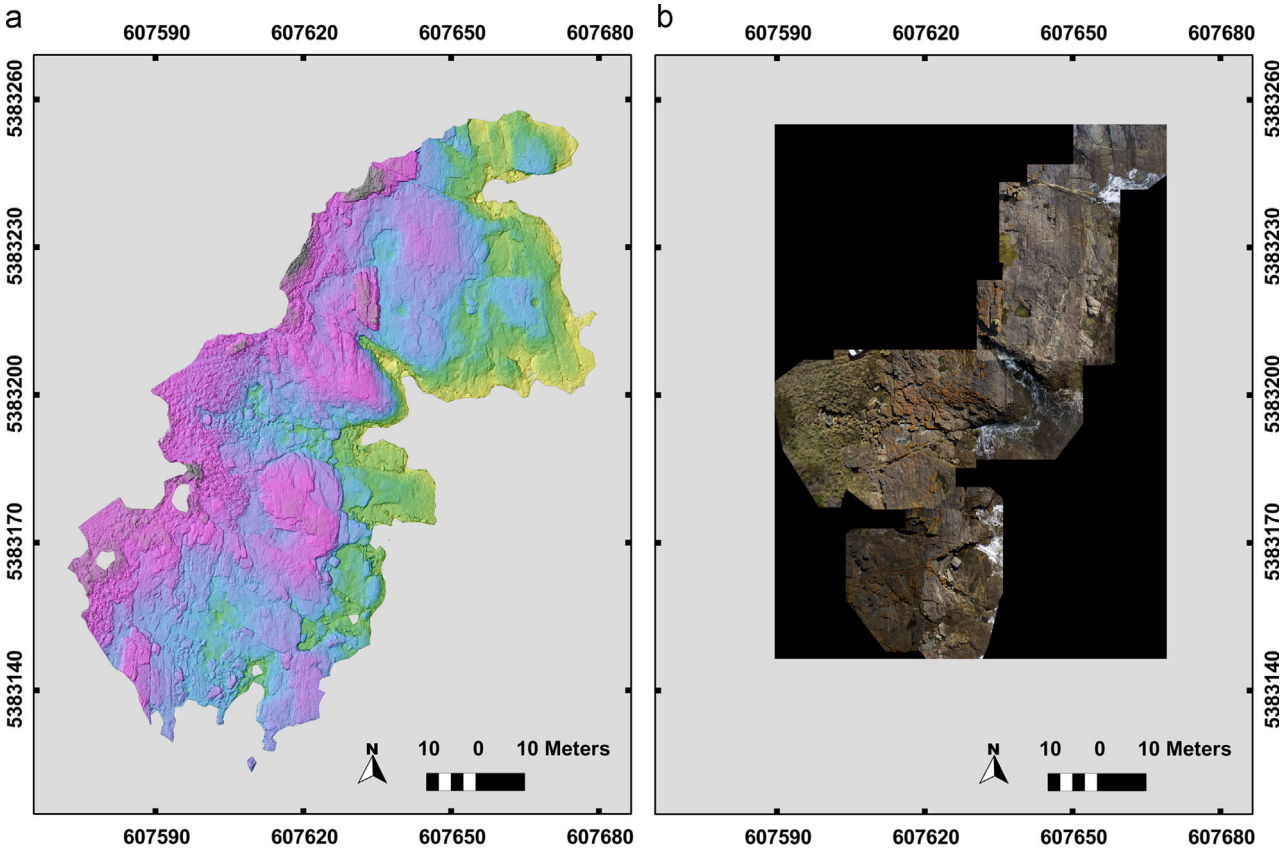


Fig. 2. (a) DEM. (b) Photomosaic.

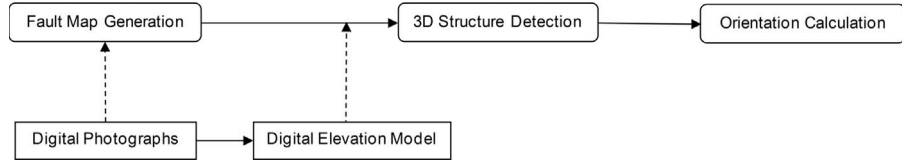


Fig. 3. Overview of workflow.

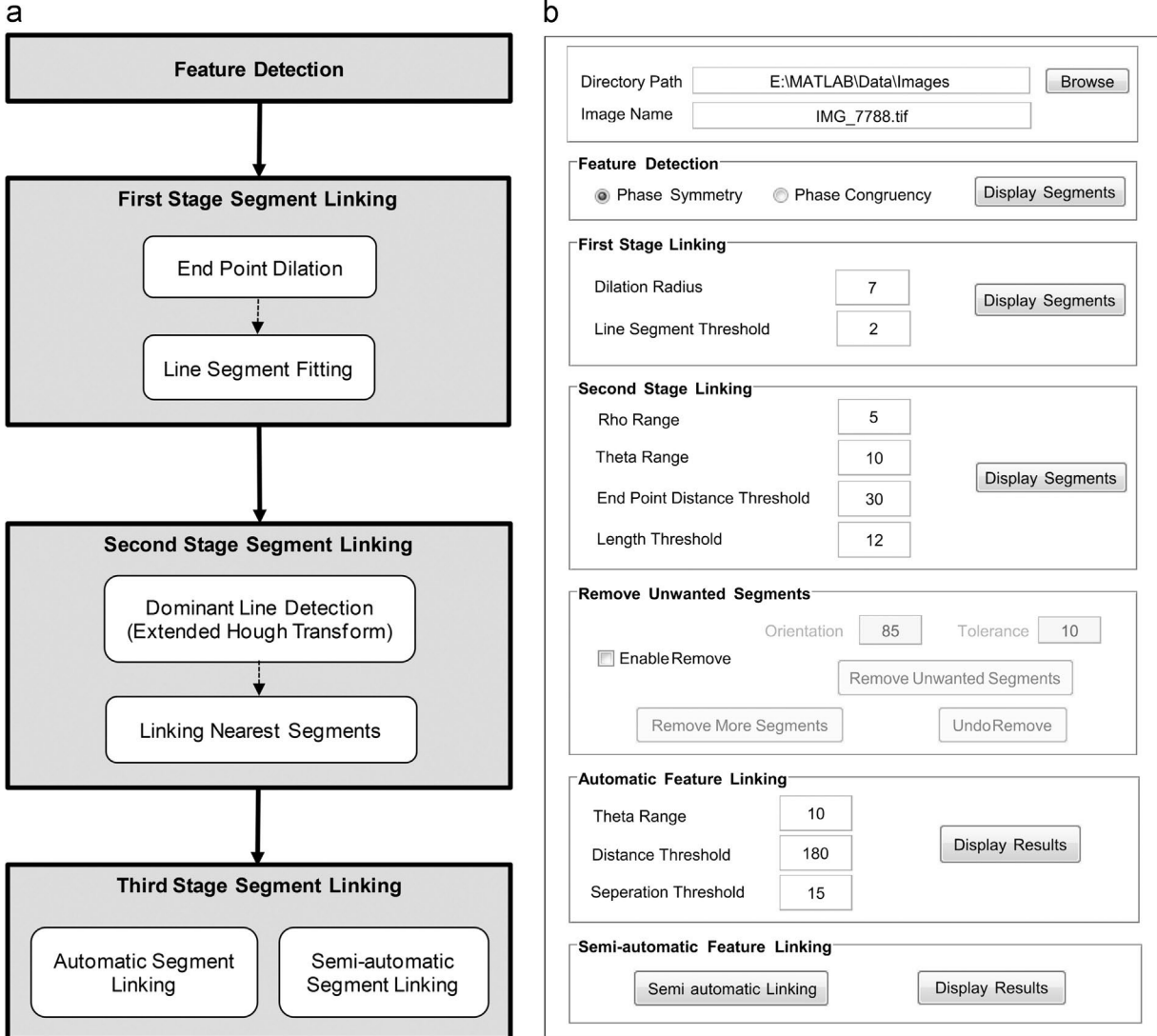


Fig. 4. (a) Structure map generation workflow. (b) Graphical user interface for 2D structure detection.

discontinuity (Holden et al., 2008). One advantage of this method is that it is invariant to local signal strength. In this method, the axis of a line corresponds to pixels that are symmetric along different profiles sampled from all orientations other than parallel orientation. The axis of symmetry in the spatial domain corresponds to the points where all the frequency components are at either a maximum or minimum. In this algorithm axis of symmetry is identified by performing frequency analysis of the signal based on complex valued Log-Gabor filters. Details of this algorithm can be found in Kovesi (1997) and a MATLAB implementation is available in Kovesi (2000).

The phase congruency method (Kovesi, 1999) is a edge detection method that detects features by identifying points where the Fourier components are maximally in phase. Phase congruency provides a measure that is invariant to the magnitude of the signal.

Phase congruency can be used to detect edges from the images. This algorithm is detailed in Kovesi (1999, 2002, 2003) and a MATLAB implementation is available in Kovesi (2000).

Features were first detected by applying both the phase congruency and phase symmetry algorithms to the high-resolution geo-referenced photographs (Fig. 5) captured by the UAV platform. The output was then processed to thin edges/ridges and then thresholded to delineate edge/ridge pixels from others. Features were thinned by using the non-maximal suppression technique that suppresses pixels which are not part of the local-maxima. Then the thinned output was thresholded using hysteresis thresholding, which marks all pixels with values above a high threshold as “edges/ridges” and rejects all the pixels with values below a low threshold. The remaining intermediate pixels are marked as edges/ridges only if they are connected to the high threshold pixels (Canny, 1986). The results are shown in Fig. 6.

Fig. 7 shows edge detection results using the Canny algorithm. Results of Canny and contrast invariant methods differ in that the Canny method detects most of the features as two edges due to the thickness of the geological features. The Canny detector is designed to find step-like edges and thus marks a feature on both sides of the dark lines formed by shadows cast by the fractures in the rock surface. In contrast, the phase symmetry and the phase congruency detect these fractures as single features.

Both phase congruency and phase symmetry algorithms detect most features but phase congruency detects more noise as well which shows the phase symmetry algorithm is a better choice for this particular dataset. Thus, in the rest of this study we used the phase symmetry algorithm to detect ridge features representing faults in the UAV images. However in our software both of those algorithms are provided, so that the user is able to select between either phase symmetry to detect dark ridges or phase congruency

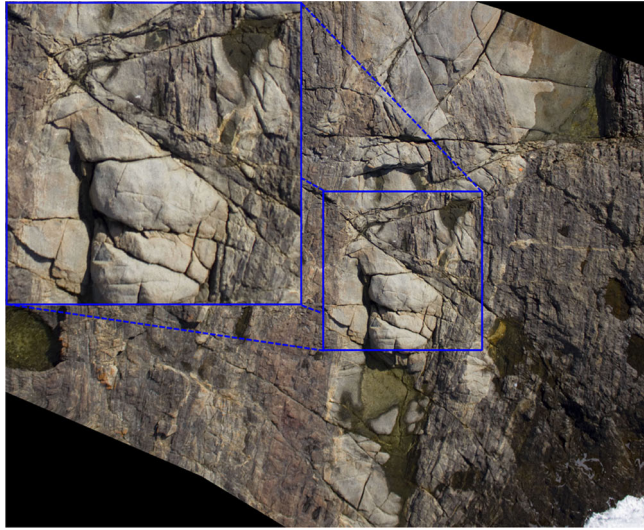


Fig. 5. Sample high resolution (1 pixel ≈ 1 cm) digital photograph taken from northern half of study site, which covers metasediments and felsic dikes. This photo covers approximately 24 m by 20 m area. A small region is enlarged for better visualisation.

to detect both visually faint and strong edges from UAV images. Note that the results from any other edge detection method can also be used in the following processes to detect the geological structures.

Geological images are challenging media on which to perform image analysis. Aerial images are affected by noise due to camera shake, low resolution image capture, shadows of other structures and the nature of surface contrast. Hence, geological lineaments often appear as discontinuous line segments on original images as shown in **Fig. 6**. During typical manual detection and digitising approaches, geologists use their knowledge and experience to determine which segments should be connected and which are not. To detect the structures effectively in an automated method, the line segments from the same structure need to be connected.

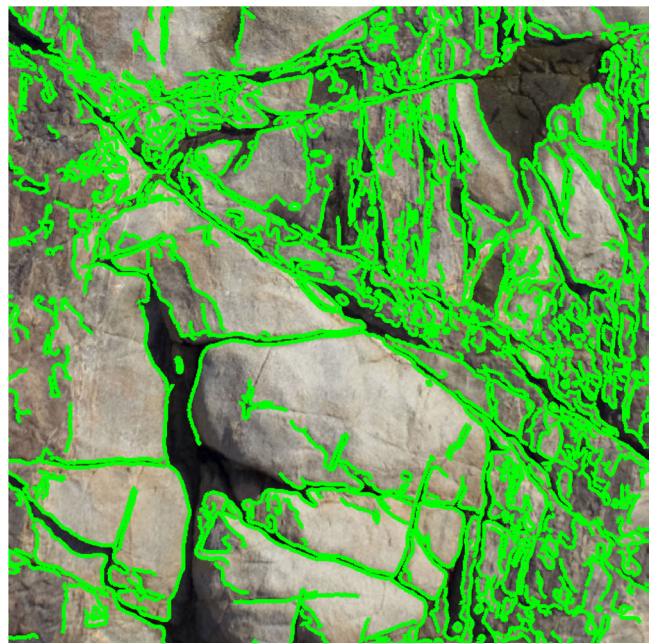


Fig. 7. Feature detection results using the Canny edge detection method.

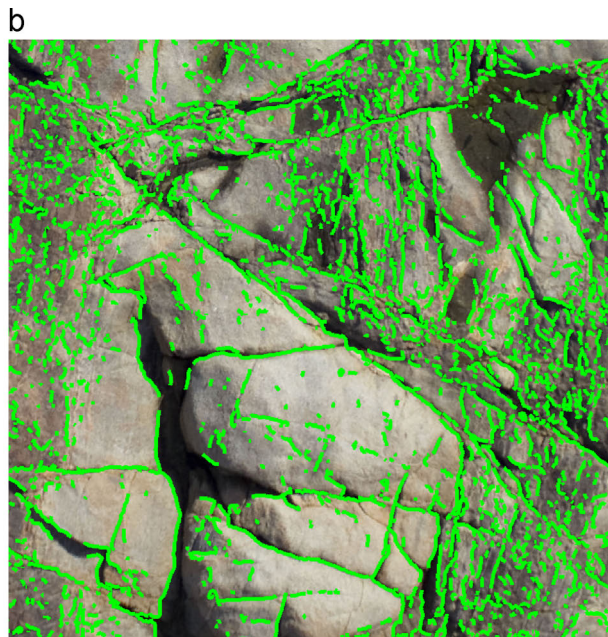
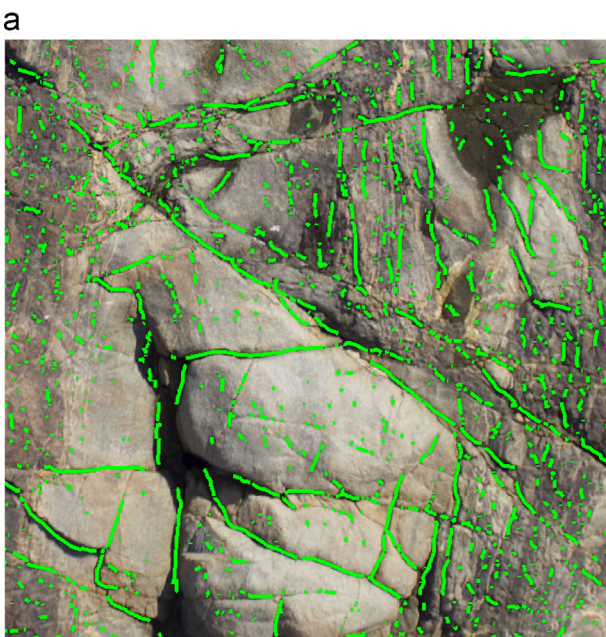


Fig. 6. Feature detection results from magnified region in **Fig. 5** using (a) Phase symmetry ridge detection and (b) phase congruency edge detection.

This makes automated lineament detection a challenging task. Two adjacent segments may come from a single structure or they can originate from two different structures. It is very difficult to distinguish them just based on the distance between the end points of those segments or based on the orientation of the line segments. In order to address this problem we have implemented the segment linking algorithm in three stages.

3.2. First stage segment linking

Morphological dilation followed by thinning can be used to fill in small gaps between nearby feature segments. In the first stage of segment linking, the endpoints of feature segments were identified and dilation was performed only at the endpoints to connect the endpoints of nearby features. A structuring element with a neighbourhood radius of 7 pixels was used to dilate the feature endpoints. This dilation causes nearby endpoints to become linked, subsequent thinning then leaves a residual line that connects the nearby endpoints together. For isolated endpoints that do not get linked to any other line segment the subsequent thinning restores the endpoints to their pre-dilated state. Connected feature pixels were linked together and then represented as a series of line segments that were fitted to the feature pixels within a specified tolerance. The line segment fitted image was post processed to remove the isolated segments that were shorter than a certain threshold. The result is shown in Fig. 8.

3.3. Second stage segment linking

While small discontinuities in edge segments can be joined with dilation and thinning operations the nature of the surfaces being viewed are such that geological lineaments will inevitably appear as a series of line segments that may be separated by a significant distance (example Fig. 8). In the second stage of segment linking, line segments that lie close to each other, having a very high probability of originating from the same structure, are connected together. A modified Hough transform method is used to find the probability.

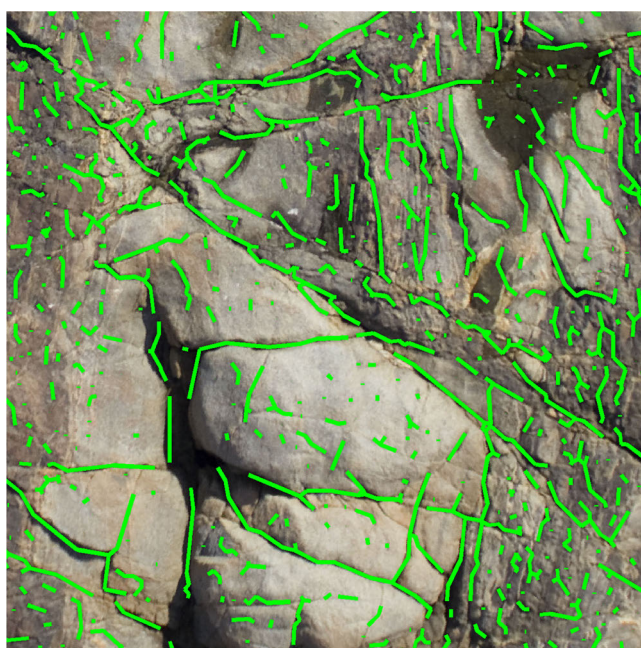


Fig. 8. Detected features after first stage segment linking, using phase symmetry ridges.

The Hough transform (Duda and Hart, 1972) is a widely used method for extracting dominant lines in edge images. However in its basic form the original Hough transform is prone to noise, since irrelevant pixels will contribute the same amount to the accumulator array. In its original form the Hough transform is not suitable for detecting lineaments within remotely sensed images as they contain a high degree of noise. Vassilas et al. (2002) proposed the use of the weighted Hough transform to overcome this problem. Even though their method was more efficient than the original Hough transform, it failed to identify lineaments in certain directions. In this study, the use of the Hough transform method is adapted and extended to identify line segments that belong to the same structure. This was achieved by mapping the detected line segments (rather than edge pixels) into the Hough space (see Fig. 9). This allowed segments that have similar orientation, θ , and perpendicular distance from origin, ρ , to be readily identified. The dominant line is detected from the image using this extended Hough Transform. The line segments which have similar ρ and θ are grouped together and connected, based on the distance between the segments (if they are below a certain threshold). The linked segments are marked as having been processed and the next unprocessed dominant segment is then selected and this process is repeated until all the feature segments are linked. The line segment fitted image was post processed to remove the segment which is shorter than a threshold (For this example 12 pixel length) (Fig. 10)

3.4. Third stage segment linking

In the third stage, segment linkage proceeds either by an automated algorithm or semi-automatically, guided by user inputs. Before linking the segments using the automated method, segments were removed from the population on the basis of their orientation. For this particular image segments with an average orientation greater than 75° relative to the horizontal direction were removed since there are no faults present in this image with that range of orientations, instead such features are mostly parallel bedding joints (Fig. 11a). The automated algorithm then identifies the longest feature segment and the segments sharing similar orientation with the longest segment. The segments with a perpendicular distance from the longest segment below a threshold are grouped together with the longest segment. Then these segments are linked together if their separations and lateral alignments are within a specified tolerance. The linked segments are marked as having been processed and the next unprocessed longest segment is selected and this process is repeated until all the segments are linked (Fig. 11b).

The automated method successfully detected most faults, joints and bedding surfaces. However some non-features were detected as features (false positives) and some features were not detected by the automated method (false negatives). Also some single features are detected as two or more, shorter length features.

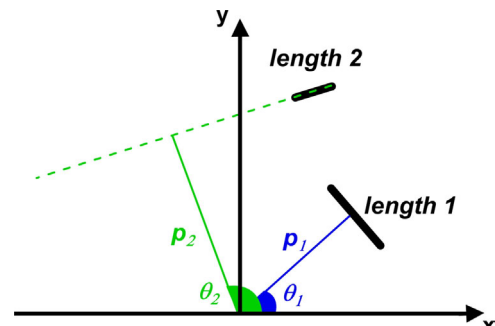


Fig. 9. Modified Hough transform parameters applied to line segments.

To quantify the performance of our algorithm the results were compared with the fault map (Fig. 12) resulting from a visual interpretation by an expert who had visited the outcrop. Note that the automated method detects faults, joints and jointed bedding surface while the visual interpretation shows only the faults. We use recall to quantify the comparison.

$$R_a = \frac{L_a}{L_v}$$

where L_a represents the total length of faults common to the automated results and the visual interpretation and L_v represents the total length of faults on visual interpretation. For this particular area L_a is 15,917 cm, L_v is 24,653 cm and the recall is 64.5%.

Geological analysis of images is not a trivial process as it requires the interpretation of complex geometries and subtle colour changes. Their analysis requires significant intuition, deductive and inductive reasoning of the interpreter. Thus, it is important that human interaction is allowed to ensure the output is geologically feasible.

In our method, user has the option of interpreting the image using a semi-automated algorithm, which allows the

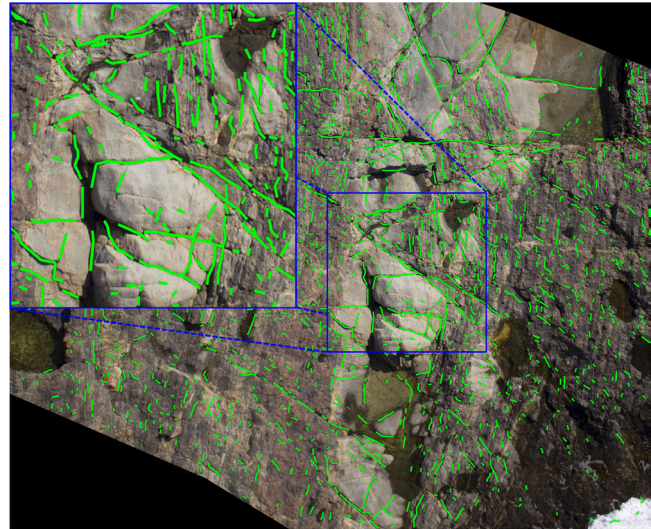


Fig. 10. Detected feature segments after second stage of segment linking.

interpreters to interact and produce geologically feasible results. In this method the segment detection result (Fig. 10) is displayed and the users are asked to select the features by clicking mouse button roughly along the features. The user needs to click the left mouse button at a small number of locations along a structure until their selection is completed by pressing the right mouse button. This process is repeated until the user selects all the structures. In order to avoid the selection of the same structure multiple times, the clicked points are linked together using straight lines as soon as the user completes the selection of a structure. Fig. 13a shows the user clicked locations (red squares) and the linked lines in green colour overlaid on top of the original image. Then finally, the segments lying near the user interpreted lines are grouped together and linked together to form the final semi-automated feature map (Fig. 13b).

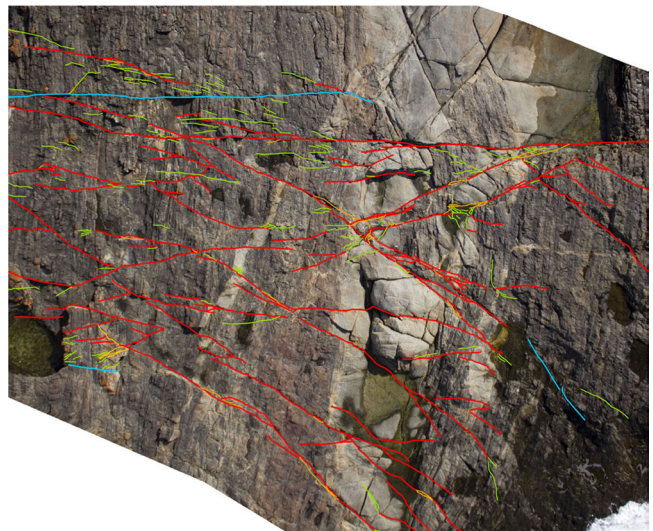


Fig. 12. Fault map, resulting from visual interpretation, where different colours indicate different fracture type. A red colour was used to mark faults, in which offset could be seen clearly in the photo. A green colour was used for extension fractures, cyan lines indicates joints and an orange colour indicates faulting and extension fracturing at step-overs. The interpretation of fracture types are scale dependant (depend on the resolution of images). (For interpretation of the references to colour in this figure legend, the reader is referred to the web version of this article.)

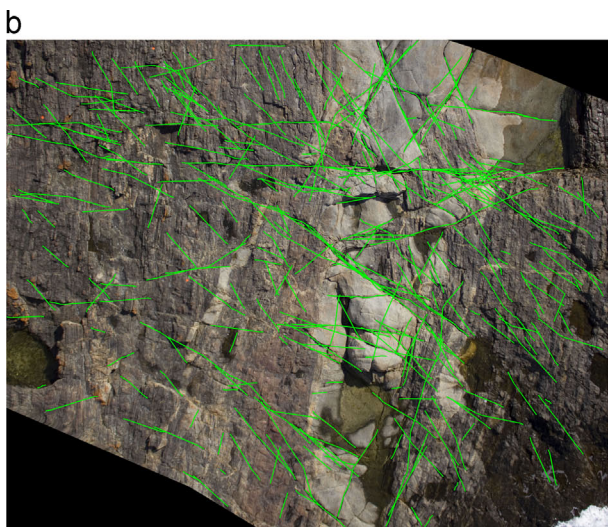
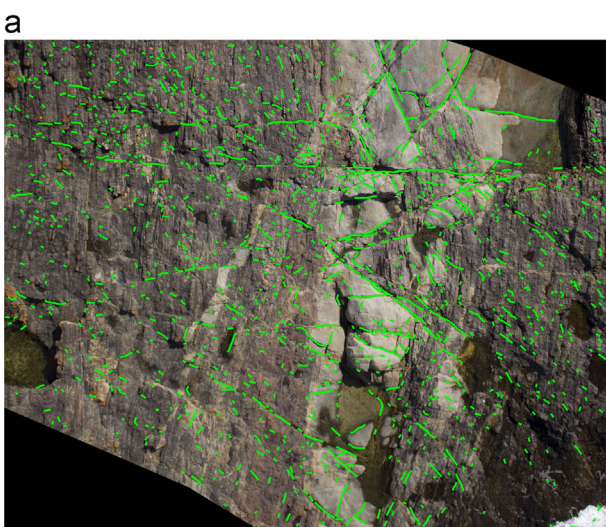


Fig. 11. (a) Feature segments, after segments from an unwanted orientation range were removed (in this case segment orientations greater than 75°). (b) Detected faults, joints and bedding surfaces by our automated method.

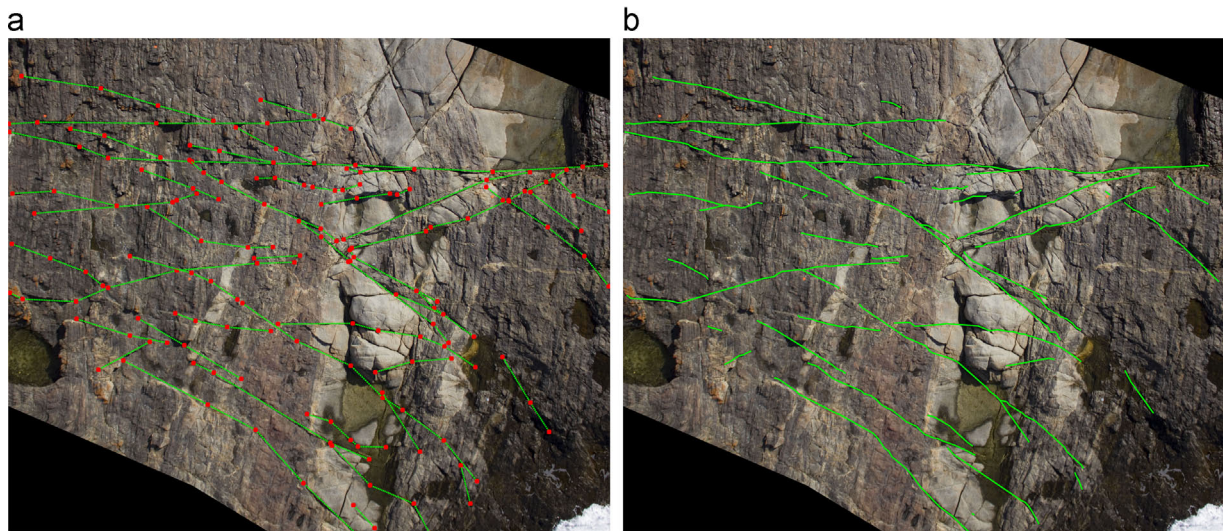


Fig. 13. (a) User clicked locations for semi automatic interpretation where mouse click locations are shown as red colour squares. (b) Fault map, resulting from semi-automated method. (For interpretation of the references to colour in this figure legend, the reader is referred to the web version of this article.)

This process is relatively easy and a time-efficient task for the user since almost all the features are highlighted in the displayed image based on the segment detection results. Furthermore, in conventional visual interpretations, the user has to carefully interpret the bends/stopovers, whereas in the semi-automated method they just need to click on a limited set of locations without worrying about the bends as the semi-automated method will automatically detect the faults with realistic geometries, including bends/stopovers, closely spaced parallel faults, intersections and tip zone splays (Fig. 13b).

3.5. Comparison of semi-automatic fault map with manually interpreted map

For better visual comparison of the locations of the faults identified by both semi-automated and visual methods, the faults detected by the semi-automated method were plotted on top of the visually interpreted fault map (Fig. 14). Please note that not all the features were considered during the semi-automatic mapping exercise that had been identified by the original visual interpretation (especially the extension fractures). The results show that of the faults, identified using the semi-automated method the majority maintain a very similar geometry and are in the same locations as the faults mapped by the visual interpretation.

To determine the effectiveness of our semi-automated method, the results are compared with the visual interpretation results. Recall of semi-automated method is calculated as

$$R_{sa} = \frac{L_{sa}}{L_{vg}}$$

where L_{sa} is the total length of the faults identified in the semi-automated method and L_{vg} is the total length of faults identified in visual interpretation. However as explained above some of the faults identified in the visual interpretation were not considered by the user in the semi-automated method. Thus we did not include the lengths of those fractures when calculating L_{vg} . For this area L_{sa} is 17,680 cm, L_{vg} is 22,154 cm which gives a recall of 79.8%.

Some features that are correctly mapped by the semi-automated method are shorter than in the visual interpretation, since some of the faint edges were not detected by the edge detection algorithms. A little more time investment on behalf of the user may well have solved this issue, with the shorter features being restricted by the user's choice of points. Notwithstanding

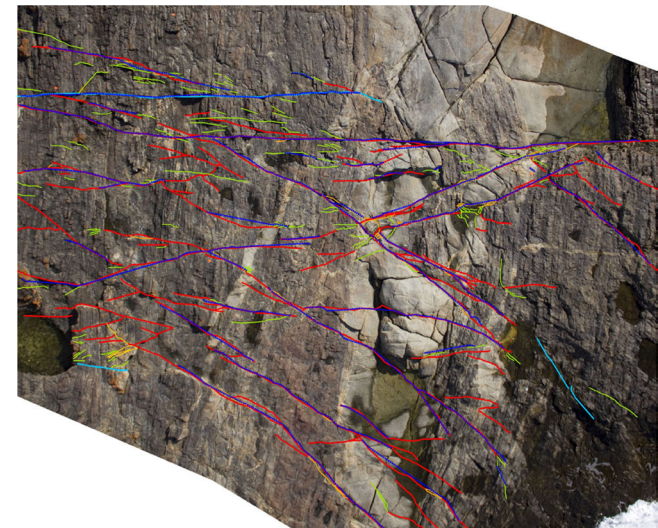


Fig. 14. Faults detected by the semi-automated method (blue colour line) were plotted on top of the fault map from Fig. 12, resulting from visual interpretation for visual comparison. Please note that all the faults identified by visual interpretation are not guided in the semi-automated method. (For interpretation of the references to colour in this figure legend, the reader is referred to the web version of this article.)

this, the average time taken for semi-automated interpretation was 10 min, while it took ~7 h to interpret the image visually in standard geographic information software.

4. Automated 3D structure analysis

4.1. 3D structure detection

Once the structures are identified in the 2D images the 2D feature points $X2d$, $Y2d$ (pixel coordinates) are computed and their corresponding 3D feature coordinates ($X3d$, $Y3d$) are calculated. The Z coordinate of the feature point, $Z3d$ was calculated from the DEM using bilinear interpolation. This approach requires the 2D images to be orthorectified. Note that the output of the bundle adjustment process provides the camera location and calibration parameters. If the images are not orthorectified, these can be used

to project a viewing ray corresponding to a feature location in the 2D image into the 3D surface. The intersections with the 3D surface will give the 3D location of the feature points.

4.2. Orientation calculation

Once the 3D feature points are computed, the discontinuity plane was extracted to estimate dip and dip direction of the structure. We use the Random sample consensus (RANSAC) (Fischler and Bolles, 1981) algorithm to identify best fit planes from the given dataset. Alternately, least squares fitting methods can be used to identify planes from the 3D feature points but the results will be accurate only if the dataset is outlier free. The 3D point cloud will contain data belonging to several planes, and will also inevitably contain some noise. If a least squares method is used to fit a plane, large plane fitting errors will arise, even with a small percentage of outliers. Thus, it is essential to first remove the outliers before applying the least square fitting method. It is capable of fitting models to data with a large percentage of outliers; about 50% outliers can be handled routinely.

The RANSAC algorithm initially identifies the model (in our study it is plane) with a randomly selected minimum number of points, which is 3 in the case of a plane. The distance between each point in the dataset and the plane is computed and if the distance is below a threshold then those points are considered as inliers. Otherwise they are considered as outliers. The random selection of points is repeated several times and the model with largest consensus set is taken to be the correct model. In this study the RANSAC algorithm is used to identify the best-fit plane, in a methodology similar to Ferrero et al. (2009). Note that it is only possible to fit a plane if the 3D data points are not degenerate, that is if they do not lie in a straight line. Degeneracies arise where a configuration does not have a unique solution. Thus, RANSAC will fail to find a correct model in the presence of degenerate configuration (Hartley and Zisserman, 2004).

Once the coefficients of the best-fit plane are identified it is relatively straight-forward to extract orientation measurements such as dip and dip direction. The equation of the best-fit plane can be defined by

$$ax + by + cz + d = 0$$

where a , b , c and d are the coefficients of the best-fit plane.



Fig. 15. Survey locations.

The dip and dip direction of this best-fit plane can be written as

$$\text{Dip} = \arccos \left| \frac{c}{\sqrt{a^2 + b^2 + c^2}} \right|$$

$$\text{Dip direction} = k \pm \arccos \left(\frac{a}{\sqrt{a^2 + b^2}} \right)$$

where k is 0° or 180° or 360° depending on the quadrant (Feng et al., 2001).

4.3. Comparison of orientation data with field measurements

A field survey was conducted in the study area and the dip and dip direction of a single, well-exposed fault were measured at ten locations along the fault (Fig. 15), using a compass-clinometer aligned directly against the plane of exposed fault surfaces. We compare these field measurements against orientations calculated from the digital data at the same locations using an automated method, described in Section 3.4. It is not possible to define a plane using only one point instead using the automated method, we need a line segment that is at least 3 pixel lengths to calculate fault orientation at each location. These line segments are centred at the locations where the field measurements were made, and we calculated their dip and dip directions using different length line segments to test the robustness of the results. The results are presented in Fig. 16.

The results show that the calculated orientations, using the automated method match well with the field data. Further analysis was performed based on the absolute difference in dip and dip direction calculation using different pixel lengths. The results (Fig. 17a) show that the dip calculated with a fault segment where length is greater than 21 pixels (21 cm) shows more realistic results and Fig. 17b shows that the dip direction (or strike) calculated using 21 pixel length fault segment has the best fit with the field data. The automated method results using 21 pixel length segments are presented in Table 1. The mean \pm standard error of the absolute differences in dip calculation is $1.9^\circ \pm 2.2^\circ$ and the dip direction calculation is $4.4^\circ \pm 2.6^\circ$. It is generally accepted that field measurements vary by $3\text{--}5^\circ$ between different users and compass clinometers. Thus the results obtained by our automated method show the potential of using this semi-automated method for accurate and efficient measurements of orientations. Furthermore field measurements are taken by considering only a single point or a scan line but the photogrammetry method calculates the orientations from a local discontinuity plane while considering the wavy nature of the fault.

5. Conclusion

This paper outlines a method to rapidly map geological structures from photogrammetric data (such as that collected rapidly and efficiently by UAVs) and calculate their orientation using automated methods. The geological structures (faults) are detected using contrast invariant feature detection algorithm and segment linking methods. Our method produces a geologically feasible fault map while minimising the time taken for the interpretation. Our semi-automatic method improved the time taken to digitise a fault map from hours to minutes.

We demonstrate that once a fault map has been generated it is relatively easy to extract additional data, such as multiple measurements of the orientation of structures along strike. Our orientation analysis approach relies on identifying the corresponding 3D feature coordinates in the 3D surface model, with the use of a DEM derived from the original photogrammetric model. The RANSAC algorithm was used to find the best fit plane from these 3D coordinates and the dip and dip direction are calculated using

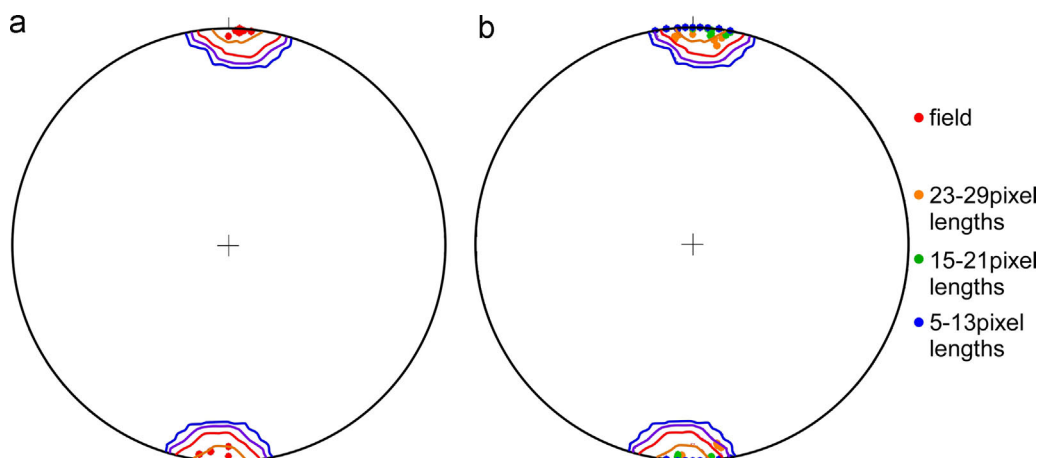


Fig. 16. Poles to fault orientations at 10 different locations along the selected structure. Data were both measured in the field (red circles) and calculated for the same 10 locations using different pixel lengths. (a) Poles and contours of measured field data. (b) Calculated fault orientations compared against field data contours. Calculations used fault lengths that were 5–13 pixels long (blue), 15–21 pixels long (orange) and 23–29 pixels long (red). All calculated data fall within the 10% contour limit of the field data, indicating that the calculated orientations match well with the field data. (For interpretation of the references to colour in this figure legend, the reader is referred to the web version of this article.)

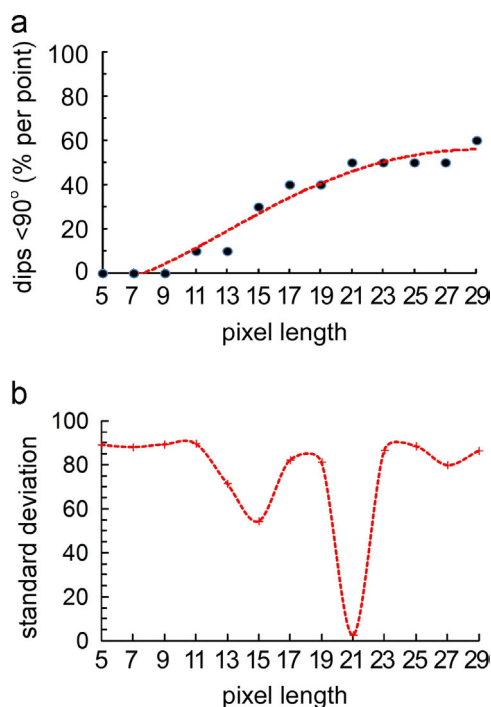


Fig. 17. Comparison between field and calculated orientation data for (a) the dip and (b) the strike of the fault orientation measurements. Note, although the field data shows the fault is steep dipping 90°, the field measurements still have dips < 90°. However there is a tendency for calculated data to derive dips of precisely 90 degrees (2 decimal places). (a) Percentage of calculated dips which are less than 90°, for different pixel lengths at each measurement location. Calculated data fit a 4th order polynomial with a shoulder at 21 pixel length, beyond which 50–60% of calculations obtain more realistic dip orientations. (b) Standard deviation of the difference between the calculated and observed fault strikes. There is a pronounced minima at 21 pixels, indicating calculations using 21 pixels have the best fit with the observed field data.

the best fit plane coefficients. Orientation calculation results from our semi-automated method compared well with the measurements obtained from a field survey with a mean \pm standard error of the absolute differences of $1.9^\circ \pm 2.2^\circ$ for dip calculation and $4.4^\circ \pm 2.6^\circ$ for the dip direction calculation.

The structure mapping and orientation analysis techniques outlined in this paper are particularly useful to map structures from photogrammetric models of sites, which are normally inaccessible.

Table 1

Discontinuity (fault) segment orientation obtained with the traditional method and our automated method.

| Survey locations | Field measurement | | Photogrammetry measurement | | Absolute difference | |
|------------------|-------------------|---------------|----------------------------|---------------|---------------------|---------------|
| | Dip | Dip direction | Dip | Dip direction | Dip | Dip direction |
| P1 | 82 | 0 | 88 | 355 | 6 | 5 |
| P2 | 87 | 0 | 90 | 358 | 3 | 2 |
| P3 | 87 | 8 | 87 | 4 | 0 | 4 |
| P4 | 89 | 186 | 90 | 187 | 1 | 1 |
| P5 | 89 | 182 | 87 | 189 | 2 | 7 |
| P6 | 89 | 184 | 89 | 180 | 0 | 4 |
| P7 | 88 | 183 | 90 | 180 | 2 | 3 |
| P8 | 85 | 5 | 90 | 2 | 5 | 3 |
| P9 | 86 | 180 | 86 | 185 | 0 | 5 |
| P10 | 90 | 183 | 90 | 173 | 0 | 10 |

This includes remote sensing surveys of planetary geology, active and inactive open pit mine sites, vulcanological surveys of hazardous calderas or geological surveys of coastal and mountain cliffs. This tool may be particularly useful to geomorphologists, mine geologists and geotechnical engineers who are analysing for slope stability or landslide hazard assessment.

Acknowledgements

We would like to acknowledge Darren Turner and Arko Lucieer, University of Tasmania, who flew the UAV survey and generated the surface models used in this study. We also acknowledge The University of Western Australia for providing a Scholarship for International Research Fees (SIRF) for this study.

References

- Abdullah, A., Nassr, S., Ghaleeb, A., 2013. Landsat ETM-7 for lineament mapping using automatic extraction technique in the SW part of Taiz Area, Yemen. *Global J. Hum. Soc. Sci. Res.* 13, 35–38.
- Argialas, D.P., Mavrantza, O.D., 2004. Comparison of edge detection and hough transform techniques for the extraction of geologic features. *Int. Arch. Photogramm. Remote Sens. Spat. Inf. Sci.* 34, 790–795.
- Canny, J., 1986. A computational approach to edge detection. *IEEE Trans. Pattern Anal. Mach. Intell.* PAMI-8, 679–698, <http://dx.doi.org/10.1109/TPAMI.1986.4767851>.

- Den Hertog, A.L., Visser, D.W., Ingham, C.J., Fey, F.H.A.G., Klatser, P.R., Anthony, R.M., 2010. Simplified automated image analysis for detection and phenotyping of mycobacterium tuberculosis on porous supports by monitoring growing microcolonies. *PLoS ONE* 5, e11008, <http://dx.doi.org/10.1371/journal.pone.0011008>.
- Donovan, J., LeBaron, A., 2009. A comparison of photogrammetry and laser scanning for the purpose of automated rock mass characterization. Presented at the 43rd U.S. Rock Mechanics Symposium & 4th U.S.-Canada Rock Mechanics Symposium. American Rock Mechanics Association.
- Duda, R.O., Hart, P.E., 1972. Use of the Hough transformation to detect lines and curves in pictures. *Commun. ACM* 15, 11–15, <http://dx.doi.org/10.1145/361237.361242>.
- Feng, Q., Sjogren, P., Stephansson, O., Jing, L., 2001. Measuring fracture orientation at exposed rock faces by using a non-reflector total station. *Eng. Geol.* 59, 133–146, [http://dx.doi.org/10.1016/S0013-7952\(00\)00070-3](http://dx.doi.org/10.1016/S0013-7952(00)00070-3).
- Ferrero, A., Forlani, G., Roncella, R., Voyat, H., 2009. Advanced geostructural survey methods applied to rock mass characterization. *Rock Mech. Rock Eng.* 42, 631–665, <http://dx.doi.org/10.1007/s00603-008-0010-4>.
- Ferrero, A.M., Migliazza, M., Roncella, R., Segalini, A., 2011. Rock cliffs hazard analysis based on remote geostructural surveys: the Campione del Garda case study (Lake Garda, Northern Italy). *Geomorphology* 125, 457–471, <http://dx.doi.org/10.1016/j.geomorph.2010.10.009>.
- Fischler, M.A., Bolles, R.C., 1981. Random sample consensus: a paradigm for model fitting with applications to image analysis and automated cartography. *Commun. ACM* 24, 381–395.
- Furukawa, Y., Ponce, J., 2010. Accurate, dense, and robust multiview stereopsis. *IEEE Trans. Pattern Anal. Mach. Intell.* 32, 1362–1376.
- Gustafsson, P., 1994. Spot satellite data for exploration of fractured aquifers in a semi-arid area in Southeastern Botswana. *Appl. Hydrogeol.* 2, 9–18, <http://dx.doi.org/10.1007/s100400050246>.
- Haneberg, W.C., 2008. Using close range terrestrial digital photogrammetry for 3-D rock slope modeling and discontinuity mapping in the United States. *Bull. Eng. Geol. Environ.* 67, 457–469, <http://dx.doi.org/10.1007/s10064-008-0157-y>.
- Hartley, R., Zisserman, A., 2004. *Multiple View Geometry in Computer Vision*, 2nd ed. Cambridge University Press.
- Harwin, S., Lucieer, A., 2012. Assessing the accuracy of georeferenced point clouds produced via multi-view stereopsis from Unmanned Aerial Vehicle (UAV) imagery. *Remote Sens.* 4, 1573–1599, <http://dx.doi.org/10.3390/rs4061573>.
- Holden, E.-J., Dentith, M., Kovesi, P., 2008. Towards the automated analysis of regional aeromagnetic data to identify regions prospective for gold deposits. *Comput. Geosci.* 34, 1505–1513, <http://dx.doi.org/10.1016/j.cageo.2007.08.007>.
- Hung, L.Q., Batelaan, O., De Smedt, F., 2005. Lineament extraction and analysis, comparison of LANDSAT ETM and ASTER imagery. Case study: suoimuoii tropical karst catchment, Vietnam, vol. 5983. In: Proceedings of SPIE. Presented at the Remote Sensing for Environmental Monitoring, GIS Applications, and Geology, SPIE. pp. 59830T-1–59830T-12, <http://dx.doi.org/10.1117/12.627699>.
- Irschara, A., Kaufmann, V., Klopschitz, M., Bischof, H., Leberl, F., 2010. Towards fully automatic photogrammetric reconstruction using digital images taken from UAVs. In: Proceedings of the ISPRS TC VII Symposium—100 Years ISPRS.
- Juneja, M., Sandhu, P.S., 2009. Performance evaluation of edge detection techniques for images in spatial domain. *Int. J.* 1, 614–621.
- Kottenstette, J., 2005. Measurement of geologic features using close range terrestrial photogrammetry. In: Proceedings of the 40th US Symposium on Rock Mechanics (USRMS) Alaska Rocks 2005.
- Kovesi, P., 1997. Symmetry and asymmetry from local phase. In: Proceedings of the Tenth Australian Joint Conference on Artificial Intelligence. pp. 2–4.
- Kovesi, P., 1999. Image Features from Phase Congruency. *Videre: J. Comput. Vis. Res.* 1, 1–26.
- Kovesi, P., 2000. MATLAB and Octave Functions for Computer Vision and Image Processing.
- Kovesi, P., 2002. Edges are not just steps. In: Proceedings of the Fifth Asian Conference on Computer Vision. pp. 822–827.
- Kovesi, P., 2003. Phase congruency detects corners and edges. In: Proceedings of the Australian Pattern Recognition Society Conference. pp. 309–318.
- Lemy, F., Hadjigeorgiou, J., 2003. Discontinuity trace map construction using photographs of rock exposures. *Int. J. Rock Mech. Min. Sci.* 40, 903–917, [http://dx.doi.org/10.1016/S1365-1609\(03\)00069-8](http://dx.doi.org/10.1016/S1365-1609(03)00069-8).
- Linder, W., 2009. *Digital Photogrammetry: A Practical Course*, 3rd ed. Springer.
- Lowe, D.G., 2004. Distinctive image features from scale-invariant keypoints. *Int. J. Comput. Vis.* 60, 91–110.
- Lucieer, A., Robinson, S.A., Turner, D., 2011. Unmanned Aerial Vehicle (UAV) remote sensing for hyperspatial terrain mapping of antarctic moss beds based on Structure from Motion (SfM) point clouds. In: Proceedings of the 34th International Symposium on Remote Sensing of Environment (ISRSE34).
- Lucieer, A., Turner, D., King, D.H., Robinson, S.A., 2013. Using an Unmanned Aerial Vehicle (UAV) to capture micro-topography of Antarctic moss beds. *Int. J. Appl. Earth Obs. Geoinf.*, <http://dx.doi.org/10.1016/j.jag.2013.05.011>.
- Mabee, S.B., Hardcastle, K.C., Wise, D.U., 1994. A method of collecting and analyzing lineaments for regional-scale fractured-bedrock aquifer studies. *Ground Water* 32, 884–894, <http://dx.doi.org/10.1111/j.1745-6584.1994.tb00928.x>.
- Maini, R., Aggarwal, H., 2009. Study and comparison of various image edge detection techniques. *Int. J. Image Process.* 3, 1.
- Marghany, M., Mahdi, S.I.E., Hashim, M., 2006. Automatic detection of lineaments from LANDSAT Images in United Arab Emirate (UAE) – Universiti Teknologi Malaysia Institutional Repository. In: Proceedings of the International Conference on Space Technology and Geo-Informatics.
- Micklethwaite, S., Turner, D., Vasuki, Y., Kovesi, P., Holden, E.-J., Lucieer, A., 2012. Mapping from an armchair: rapid, high-resolution mapping using UAV and computer vision technology. *Struct. Geol. Resour.* 2012, 130–133.
- Mulrane, L., Rexhepaj, E., Penney, S., Callanan, J.J., Gallagher, W.M., 2008. Automated image analysis in histopathology: a valuable tool in medical diagnostics. *Expert Rev. Mol. Diagn.* 8, 707–725, <http://dx.doi.org/10.1586/14737159.8.7.707>.
- Oliver, C.J., Blacknell, D., White, R.G., 1996. Optimum edge detection in SAR. *IEE Proc. Radar Sonar Navigation* 143, 31–40, <http://dx.doi.org/10.1049/ip-rsn:19960219>.
- Onkaew, D., Turior, R., Uyyanonvara, B., Kondo, T., 2011. Automatic extraction of retinal vessels based on gradient orientation analysis. In: Proceedings of the Eighth International Joint Conference on Computer Science and JCSSE. Presented at the Eighth International Software Engineering Joint Conference on Computer Science and Software Engineering (JCSSE). pp. 102–107. <http://dx.doi.org/10.1109/JCSSE.2011.5930102>.
- Priest, S.D., 1993. *Discontinuity Analysis for Rock Engineering*. Springer.
- Sander, P., Minor, T.B., Chesley, M.M., 1997. Ground-water exploration based on lineament analysis and reproducibility tests. *Ground Water* 35, 888–894, <http://dx.doi.org/10.1111/j.1745-6584.1997.tb00157.x>.
- Sarp, G., 2005. *Lineament analysis from satellite images, northeast of Ankara (M.Sc. thesis)*. Middle East Technical University.
- Shao, Y., Guo, B., Hu, X., Di, L., 2011. Application of a fast linear feature detector to road extraction from remotely sensed imagery. *IEEE J. Sel. Topics Appl. Earth Obs. Remote Sens.* 4, 626–631, <http://dx.doi.org/10.1109/JSTARS.2010.2094181>.
- Snavely, N., Seitz, S.M., Szeliski, R., 2007. Modeling the world from internet photo collections. *Int. J. Comput. Vis.* 80, 189–210, <http://dx.doi.org/10.1007/s11263-007-0107-3>.
- Tonon, Kottenstette, 2006. *Laser and Photogrammetric Methods for Rock Face Characterization held at GoldenRocks 2006, the 41st U.S. Rock Mechanics Symposium*. Colorado School of Mines 6, 17–18.
- Treash, B.K., Amarantunga, K., 2000. Automatic road detection in grayscale aerial images. *ASCE J. Comput. Civil Eng.* 14, 60–69.
- Turner, D., Lucieer, A., Watson, C., 2012. An automated technique for generating georectified mosaics from ultra-high resolution Unmanned Aerial Vehicle (UAV) imagery, based on Structure from Motion (SfM) point clouds. *Remote Sens.* 4, 1392–1410, <http://dx.doi.org/10.3390/rs4051392>.
- Vassilas, N., Perantonis, S., Charou, E., Tsenoglou, T., Stefofli, M., Varoufakis, S., 2002. Delineation of lineaments from satellite data based on efficient neural network and pattern recognition techniques. In: Proceedings of the 2nd Hellenic Conference on AI, SETN-2002. pp. 11–12.
- Vasuki, Y., Holden, E.-J., Kovesi, P., Micklethwaite, S., 2013. A geological structure mapping tool using photogrammetric data. In: ASEG Extended Abstracts. pp. 1–4.
- Wang, J., Howarth, P.J., 1990. Use of the hough transform in automated lineament. *IEEE Trans. Geosci. Remote Sens.* 28, 561–567.
- Wu, T.D., Lee, M., 2007. Geological lineament and shoreline detection in SAR images. In: Proceedings of the Geoscience and Remote Sensing Symposium, IGARSS 2007, IEEE International. pp. 520–523.